An experimental and theoretical approach on stability towards hydrolysis of triethyl phosphate and its effects on the microstructure of sol-gel-derived bioactive silicate glass

Otto Mao Vargas Machuca Bueno [a],[*],[1], Christian Leonardo Herrera [a], Celso Aparecido Bertran [a], Miguel Angel San-Miguel [a], João Henrique Lopes [b],[*],[1]

[a] Department of Physical Chemistry, Institute of Chemistry, University of Campinas – UNICAMP, P.O. Box 6154, 13083-970 Campinas, SP, Brazil
[b] Department of Chemistry, Division of Fundamental Sciences (IEF), Aeronautics Institute of Technology - ITA, 12228-900 Sao Jose dos Campos, SP, Brazil

ARTICLE INFO

ABSTRACT

The sol-gel method is versatile and one of the well-established synthetic approaches for preparing bioactive glass with improved microstructure. In a successful approach, alkoxide precursors undergo rapid hydrolysis, followed by immediate condensation leading to the formation of three-dimensional gels. On the other hand, a slow kinetics rate for hydrolysis of one or more alkoxide precursors generates a mismatch in the progression of the consecutive reactions of the sol-gel process, which makes it difficult to form homogeneous multicomponent glass products. The amorphous phase separation (APS) into the gel is thermodynamically unstable and tends to transform into a crystalline form during the calcination step of xerogel. In the present study, we report a combined experimental and theoretical method to investigate the stability towards hydrolysis of triethyl phosphate (TEP) and its effects on the mechanism leading to phase separation in 58S bioactive glass obtained via sol-gel route. A multitechnical approach for the experimental characterization combined with calculations of functional density theory (DFT) suggest that TEP should not undergo hydrolysis by water under acidic conditions during the formation of the sol or even in the gel phase. The activation energy barrier ($\Delta G^{\ddagger}$) showed a height of about 20 kcal·mol^{-1} for the three stages of hydrolysis and the reaction rates calculated for each stage of TEP hydrolysis were $k_{FHR} = 7.0 \times 10^{-3} s^{-1}$, $k_{SHR} = 6.8 \times 10^{-3} s^{-1}$ and $k_{THR} = 3.5 \times 10^{-3} s^{-1}$. These results show that TEP remains in the non-hydrolyzed form segregated within the xerogel matrix until its thermal decomposition in the calcination step, when P species preferentially associate with calcium ions (labile species) and other phosphate groups present nearby, forming crystalline domains of calcium pyrophosphates permeated by the silica-rich glass matrix. Together, our data expand the knowledge about the synthesis by the sol-gel method of bioactive glass and establishes a mechanism that explains the role played by the precursor source of phosphorus (TEP) in the phase separation, an event commonly observed for these biomaterials.

1. Introduction

Glass is a material of millenary origin widely present in our daily life, whatever our need, we almost always have the possibility of using it in different contexts [1,2]. Glass is any non-crystalline solid with a complete absence of long-range order within the atomic structure that exhibits a glass-transition temperature (T_g), i.e., a range of temperatures over which the glass transition occurs. [1–3]

This implies that the presence of a disordered structure and T_g are key factors to distinguish glass from other non-crystalline materials [2,4]. As a result, these aspects are crucial for obtaining materials with a vitreous structure [1,4–6]. Countless vitreous compositions for different purposes have been reported in the literature, among such compositions, bioactive glass has received attention in the biomedical field owing to the high demand for bone reconstruction or to replace skeletal defects [7–11].

By considering the preparation methods, the sol-gel route is by far the most versatile and widely used technique for obtaining bioactive
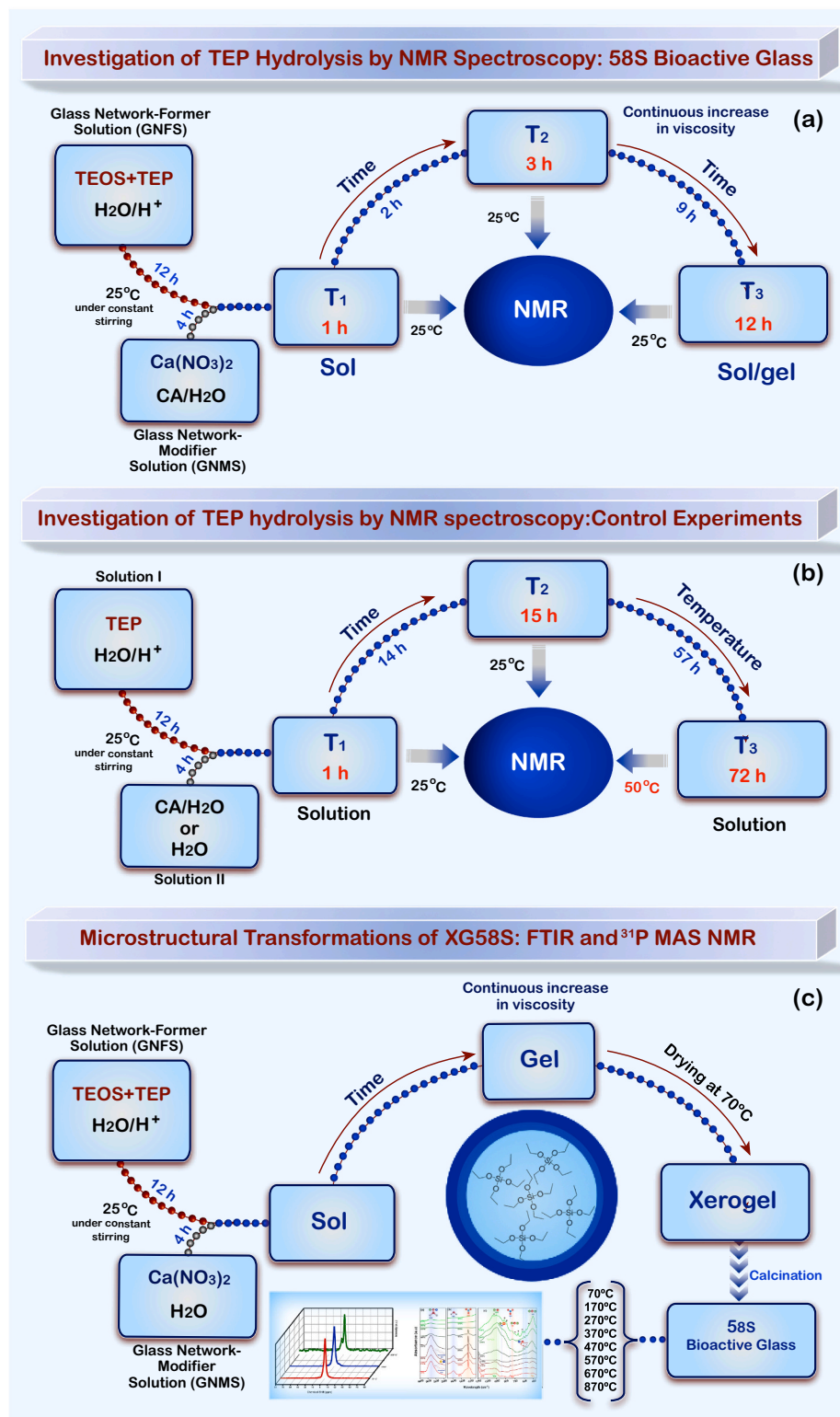

Fig. 1. Scheme summarizing all experimental steps performed in the work. Investigation of TEP hydrolysis by ^{1}H and ^{31}P NMR spectroscopy: (a) PS58S reactional brute (precursor solution of 58S bioactive glass), (b) control experiments, and (c) microstructural transformations of 58S xerogel during the calcination stage by FTIR and ^{31}P MAS NMR spectroscopy.

glass [12–17]. This method is attractive because it uses mild conditions, readily available precursors, and better structural control in terms of porosity and particle size [12,15]. Among the various bioactive glass compositions studied, 58S bioactive glass with molar composition $60SiO_2$-$36CaO$-$4P_2O_5$ (mol%) is a promising composition for bone tissue engineering [18–20]. Sol-gel-derived 58S bioactive glass is characterized by fine porous textures, enhanced degradability, and is markedly more bioactive than melt-derived glasses with the same composition [21–23]. Furthermore, in vitro studies have shown that expression of osteogenetic-relative genes, i.e., Runt-related transcription factor 2

(Runx2), collagen type I (Col I), bone sialoprotein (BSP), osteocalcin (OCN) and alkaline phosphatase (ALP) were upregulated [22,24,25].

Although the textural properties of sol-gel glass improve the apatite formation kinetics, the preparation of glassy materials with high structural homogeneity may be challenging, mainly due to the tendency of Ca and P species to be preferentially distributed into the calcium phosphate-rich phase [26,27]. In fact, a literature review demonstrates that most of the works addressing the preparation of SiO_2-P_2O_5-CaO bioactive glass via the sol-gel route leads to the formation of glass-ceramics or often basic information on the structure and thermal properties are omitted [28–30]. The presence of structural inhomogeneities changes the dissolution rate of the glass is noteworthy and undesirable from a bioactivity point of view [26,31]. Many efforts have been made in recent years to overcome this problem with relative success. An alternative sol-gel route for obtaining high structural homogeneity bioactive glass via the sol-gel route has been reported by Lopes et al. [13], in which citric acid (CA) not only served as a molecular template but also as a fuel-reducer for the self-propagating combustion. Despite these efforts, the molecular mechanisms involved in the phase separation and the formation of phosphorus-rich crystalline domains enveloped by the amorphous phase that generally arise during 58S glass-gel synthesis and similar materials are still unclear.

Herein, we report a detailed study on the long- and short-range ordering of the xerogel precursor during the calcination step and a mechanism for phase separation of 58S bioactive glass was proposed. The hypothesis is that the triethyl phosphate remains chemically unchanged during the gelling or even in the calcination step of xerogel until thermal decomposition owing to the low susceptibility of the TEP to acid-catalyzed hydrolysis. This stability towards hydrolysis of TEP may be associated with the formation of calcium phosphate clusters embedded within the glassy matrix.

It should be stressed that a complete hydrolysis for alkoxide precursors - tetraethyl orthosilicate (TEOS) and triethyl phosphate (TEP) - in an aqueous medium in the presence of a strong acid (mostly hydrochloric acid or nitric acid) has been generally accepted and widely reported in the literature [12,15,27,32,33]. This assumption is true for TEOS, while for TEP it is at least arguable. To gain insight into the phosphorus precursor behavior in sol-gel synthesis, we present a comprehensive experimental and theoretical study aiming to investigate the stability towards hydrolysis of TEP during the formation of xerogel precursor of 58S bioactive glass. In this context, functional density theory (DFT) methods represent a valuable tool with an excellent computational performance-to-cost ratio for obtaining the kinetic parameters of the chemical reactions such as TEP hydrolysis [34,35].

2. Materials and methods

2.1. Investigation of TEP hydrolysis by NMR spectroscopy

Preparation of the precursor solution involved hydrolysis reactions of stoichiometric amounts of TEOS (Si(OC$_2$H$_5$)$_4$), TEP (OP(OC$_2$H$_5$)$_3$), and calcium nitrate (Ca(NO$_3$)$_2$·4H$_2$O), as given by the nominal composition of 58S (60% SiO_2, 36% CaO, and 4% P_2O_5 in mol%) bioactive glass. All reagents and solvents were purchased from Sigma-Aldrich (Sigma-Aldrich, St. Louis, MO, USA), except the HNO_3, purchased from Synth (Labsynth, Diadema, SP, BR) and were used as received. The precursor solution was prepared by combining the so-called glass network-former solution (GNFS) and glass network-modifier solution (GNMS) as described in our previous work [13]. GNFS was obtained by hydrolyzing 20.5926 g of TEOS and 2.3584 g of TEP in 20 mL of HNO_3 (0.1 mol·L^{-1}), whereas GNMS solution was obtained by dissolving 13.732 g of (Ca(NO$_3$)$_2$·4H$_2$O) and 11.171 g of citric acid (CA) in 30 mL deionized water. Prior to combining, these solutions were vigorously stirred for 12 h at 25 °C. GNMS was slowly dripped into the GNFS, resulting in a transparent sol that from now on will be referred to as the 58S precursor solution (PS58S). PS58S was kept under vigorous stirring

and at 25 °C for investigation of TEP hydrolysis (Fig. 1a).

Nuclear Magnetic Resonance (NMR) spectroscopy was used in order to monitor and thereby predict the behavior of the triethyl phosphate within the reaction medium in the synthesis of 58S bioactive glass. Samples of the reaction media were collected and analyzed during the transformations of 58S liquid precursors in sol and, finally, in the gel network structure. For this purpose, three aliquots were extracted from the PS58S reaction medium at different times after mixing GNFS and GNMS for ^{1}H and ^{31}P NMR analysis: T$_1$ - 1 h, T$_2$ - 3 h, and T$_3$ - 12 h (Fig. 1a).

In order to gain more information on the stability towards hydrolysis of triethyl phosphate, control experiments were carried out (Fig. 1b). This experiment consists of an acidic solution of triethyl phosphate in the same concentrations as those described for the 58S precursor solution, a simplified alternative to the PS58S reaction medium. Two aliquots of TEP/H$^+$ solution were extracted for ^{1}H NMR analysis. The first after 1 h of reaction referred to as T$_1$ and the second after 15 h labeled T$_2$. Furthermore, an exploratory study to evaluate the effect of temperature on the hydrolysis reaction of triethyl phosphate by NMR was carried out in which the acid solution of TEP was maintained at 50 °C for 72 h, referred to as T$_3$.

All NMR experiments in solution were carried out by pipetting 20 μL of reaction media and which were dissolved in 700 μL of D$_2$O and collecting ^{1}H and ^{31}P spectra on the NMR spectrometers (Avance III 500 MHz (frequency for ^{1}H) or Avance III 400 MHz (frequency for ^{1}H)), Bruker, Rheinstetten/Karlsruhe, Germany Bruker.

2.2. Computational details

2.2.1. Density functional theory calculations

The quantum calculations were performed with the Gaussian quantum chemistry package 09 version D.01 [36]. Relaxed scan potential energy surface was carried out in the gas phase to find structures close to the transition state (TS) of all chemical reactions involved in the study. In all systems, the optimized geometries, harmonic vibrational frequencies, and zero-point energy (ZPE) of all the stationary points such as reactants, transition states, and products were calculated at the wB97XD/6-311++G(d,f) level of theory. Coordinating intrinsic reaction (IRC) calculations were used to verify whether TS structures would correspond to the structures of the reactive and designated products. In all cases IRC calculations were obtained with irc(calcfc, recalc = 10, maxpoints = (400 or 600), maxcycle = 40, tight, cartesian, stepsize = (7 or 5), lqa). The structures of one end of the IRC paths (reactants) were optimized to calculate the rate of reaction.

The theory of the conventional transition state (TS) was used to calculate the reaction rate constant at 298.15 K, considering the standard state in c^o = 1 M for all cases. Reaction rates were calculated for these reactions according to Eqs. (1) and (2). In all cases, the quantum mechanical tunneling effect was considered using the Wigner method [37,38].

$$K(T) = l \left[1 + \left(\frac{1}{24} \right) \left[1.44 \frac{\nu_i}{T} \right]^2 \right] \frac{K_B T}{hc^o} exp \left[\frac{-\Delta G^{\ddagger}}{RT} \right] \tag{1}$$

$$\Delta G^{\ddagger} = \sum_{TS} (E_0 + G_{corrected})_{TS} - \sum_{reactants} (E_0 + G_{corrected})_{reactants} \tag{2}$$

where l represents the reaction path degeneracy, accounting for the number of equivalent reaction paths, it is considered $l = 1$ for all calculations. h and K_b are the Planck and Boltzmann constant, respectively. V_i is the imaginary vibrational wave number in units of cm^{-1} related to the additional chemical bond of the structure of the transition state. $G^{\ddagger}$ is the activation energy barrier, E_o is the total electronic energy in $T = 0K$ and $G_{corrected}$ is the thermal correction of the Gibbs free energy. Based on the work of León-Carmona and Galano [39], the corrections Basis Set Superposition Error (BSSE) was neglected due to the overestimation of
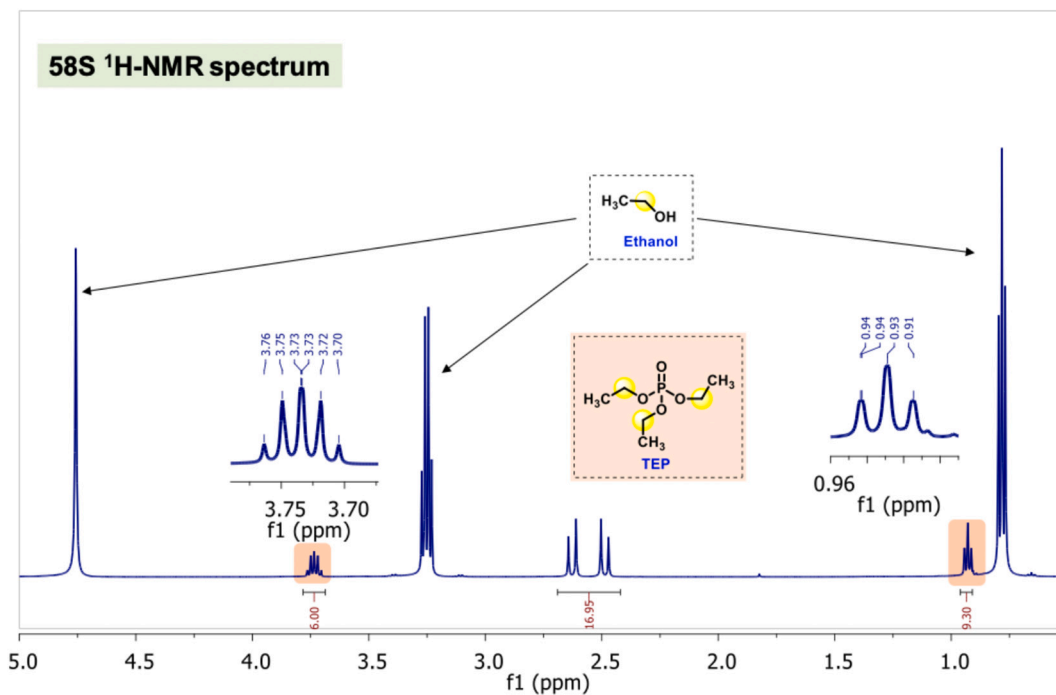
Fig. 2. ^{1}H NMR spectrum (D$_2$O, 400 MHz) for precursor sol of 58S bioactive glass in T$_1$. ^{1}H NMR spectrum shows the characteristic signals referring to methyl and methylene groups in 3.69 and 1.23 ppm, respectively. The two doublets (2.4–2.7 ppm) are related to the hydrogen present in the citric acid and singlet molecule to the water hydrogen (~4.8).

the interaction energy as shown in several works [40,41].

2.2.2. Model systems and strategy used in this work

In the DFT approach, two types of system models, continuous solvation and mixed solvency, are commonly defined to address the various studies in the literature, such as that of kinetics. However, these models predict different values for the parameters of activation energy barriers and reaction rates as reported by Ryu et al. [42]. To overcome the limitations of the continuous solvation and mixed solvency models and thereby avoiding results restricted to a model, in this work, six different types of systems were defined that cover both continuum solvation and mixed solvation as well as gas-phase systems.

In the first stage, we start with a simple gas phase system consisting of a water molecule that acts as a nucleophile and TEP molecule that contains the leaving group. Then, this system was solvated using the polarizable continuum model (PCM) solvent [43]. In the second stage, we added some explicit water molecules to favor the proton transfer mechanism, which is important in this kind of system. The addition of at least 2 water molecules, explicitly, was necessary to ensure that proton transfer occurs when the nucleophile attacks the TEP molecule. Furthermore, some water molecules were added to cover the interactions of the phosphate group, using a total of 8 water molecules explicitly. In a final stage, all previous systems were performed with implicit PCM solvation. Systems with an excess of protons were defined using the Xiao et al. [37] criteria, where the proton is placed near the active site of interest. In our case, the proton was placed near the O=P-group.

2.3. Thermal and structural characterization of 58S xerogel

Thermogravimetric analysis (TGA) of the xerogel (10 mg of the sample) was performed in a thermogravimetric analyzer (model Q50) (TA Instruments, New Castle, DE, USA). The analysis was performed under an airflow rate of 60 mL·min^{-1} in a temperature range of 30 to 1000 °C at a constant heating rate of 10 °C·min^{-1}. X-ray diffraction (XRD) patterns of 58S powders were recorded using XRD diffractograms

and collected using a diffractometer (XRD-7000, Shimadzu Scientific Instruments, Tokyo, Japan) with a Bragg Brentano camera geometry, Cu-K incident radiation (λ = 1.5418 A), 40 kV, 30 mA, and acquisition rate of 2° min^{-1} within the range 10 to 60° (2θ). The typical thermal events present in glass materials were investigated by a differential scanning calorimeter (DSC) (model DSC 6300) (SII NanoTechnology Inc., Tokyo, Japan) equipped with an EXSTAR 6000 communication device. Before DSC analysis, the xerogel was calcined at 600 °C for 60 min to remove all organic load. DSC measurements were performed on 28 mg of 58S in a platinum crucible while using analytical grade alumina powder as a reference. The conditions employed for analysis were: 10 °C·min^{-1} from room temperature up to 1100 °C under 50 mL·min^{-1} argon. The samples were heated to 10 °C above T_g before the analyses to remove residual stress and to remove any thermal history.

2.4. Effect of calcination temperature of 58S xerogel on the short-range structure by infrared spectroscopy (FTIR) and ^{31}P MAS NMR spectroscopy

The precursor xerogel of 58S (XG58S) was prepared by the hydrolysis and polycondensation of tetraethyl orthosilicate (TEOS) and triethyl phosphate (TEP), catalyzed by HNO$_3$, followed by the addition of the Ca(NO$_3$)$_2$·4H$_2$O aqueous solution. The resulting solution gives rise to sol, which progressively evolves to gel. Before reaching the gel point, the sol was poured into a Teflon® tube and aged for 12 h at room temperature (25 °C), then dried at 70 °C for 72 h. After completion of the drying step, the gels were crushed manually in an agate mortar in order to obtain a fine powder (Fig. 1c).

The microstructure transformations of XG58S as a function of the calcination temperature was investigated by Fourier transform infrared spectroscopy (FTIR) on an interferometric spectrometer operating with a ceramic bright light source and high-sensitivity DLATGS detector (Shimadzu Prestige-21, Shimadzu Corporation, Tokyo, Japan). CsI pellets were prepared by mixing 1 mg of filtered powders with 100 mg of cesium iodide and the spectra were acquired in the 4000–400 cm^{-1} region with a spectral resolution of 4 cm^{-1} and 64 scans.

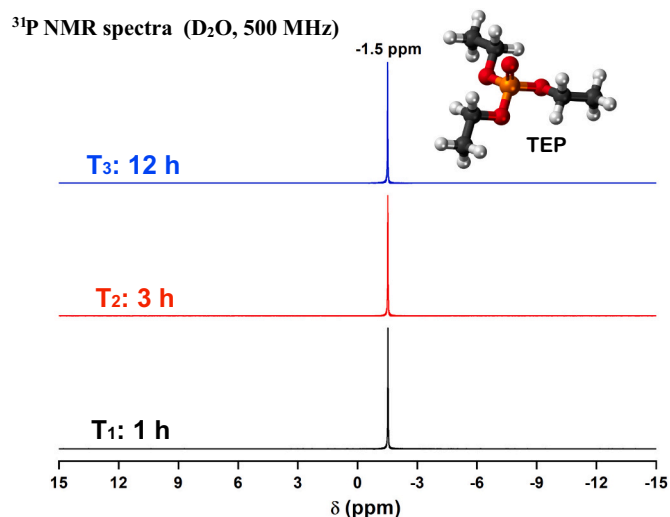^{31}P MAS NMR experiments were carried out with an FT-NMR (Bruker

Fig. 3. ^{31}P NMR spectrum (D$_2$O, 500 MHz) for precursor sol of 58S bioactive glass at different reaction times. ^{31}P NMR spectra exhibit a single signal at -1.5 ppm assigned phosphorus in the unhydrolyzed TEP molecule.

model AVANCE II+ 400) (9.04 T) (Bruker, Rheinstetten/Karlsruhe, Germany) at the resonance frequency of 161.98 using standard Bruker double-resonance magic-angle sample spinning (MAS) probes. The sample powder was packed into a 4-mm cylindrical zirconia rotor and spun at the MAS frequency at the magic angle to remove any anisotropy effects. The samples were spun at 10 kHz at the ambient probe temperature. The ^{31}P MAS experiments were obtained using a high-power decoupling (HPDEC) pulse sequence with 2.50 μs pulses, 82 ms acquisitions, 5 s recycle delays, a 100 kHz spectral width, and 1024 scans. The ^{31}P chemical shifts were referenced to 85% H$_3$PO$_4$. The spectra were processed with TopSpin 2.1.6 software using Fourier transforms and an exponential filter of 50 Hz. The phase was manually adjusted, and the baseline was obtained using a five-order polynomial function.

For these experiments, XG58S was ground using an agate mortar and pestle immediately after the drying step. The xerogel powders were then analyzed by FTIR and ^{31}P MAS NMR spectroscopy after heat treatments at different temperatures (70, 170, 270, 370, 470, 570, 670, and 870 °C), employing a heating rate of 10 °C·min^{-1} and isotherm of 60 min.

3. Results and discussion

3.1. Study of TEP hydrolysis by NMR spectroscopy

The TEP hydrolysis under acidic conditions was investigated using NMR spectrometry, which is a powerful tool that can be used to monitor the progress of chemical reactions [44] Previous works on the hydrolysis kinetics of silicon and phosphate esters over neutral, alkaline, and acidic conditions have shown considerable differences between the hydrolytic reaction rates for the TEOS and TEP compounds. [14,15,45–47] Quantitative data concerning ester bonds reactivity in organo-silicate and

-phosphate compounds revealed faster reaction kinetics for the Si-OC$_2$H$_5$ than P-OC$_2$H$_5$ bond cleavage during their hydrolyses. It has led to the assumption of complete hydrolysis for this silicon ester [13–15,45]. Although there are several works in the literature on TEOS hydrolysis, to our knowledge, this is the first study concerning TEP hydrolysis during the gel conversion and about the effects on the short- and medium-range structure of bioactive performed.

It is well known that TEP and TEOS hydrolysis reaction produces ethanol as the main byproduct, which could be easily observed in its ^{1}H NMR spectrum because of the presence of their characteristic signals referring to methyl and methylene groups in 3.69 and 1.23 ppm, respectively. In this sense, the sol-gel conversion during the preparation of bioactive glass 58S was monitored by ^{1}H NMR and ^{31}P NMR spectra analysis at different times (Fig. 1a).

Thus, we started the study comparing the ^{1}H NMR spectra of PS58S reactional brute in different times at 25 °C (Fig. 2).

As expected, 1 h after mixing GNFS and GNMS solutions (T$_1$) we observed the appearance of ethanol in the reactional brute. However, all formed ethanol could be attributed solely to TEOS hydrolysis since peaks referring to the ethoxy group of TEP (CH$_2$, δ(ppm): 3.98, dq, J_{H-P} = 8.1 Hz and CH$_3$ δ(ppm): 1.22 dt, J_{H-P} = 0.7 Hz) remained unchanged. As a result, there was no evidence of TEP hydrolysis under these acidic conditions. Similar results were observed for T$_2$ (3 h) and T$_3$ (12 h) when the gelation time was close to the end, i.e., the moment when the structure of the gel network was almost entirely formed by the aggregations of colloid particles (see the topic SM1 and Fig. SM1).

Similarly, ^{31}P NMR spectra from the reactional brute of 58S precursor solution also showed that the chemical shift of P (δ(ppm): -1.51) remained invariant during all the entire process that culminates in the formation of the gel (Fig. 3).

The stoichiometric ratio between citric acid and TEP during different times (from T$_1$ to T$_3$), calculated by the correlation of integration areas referent to methylene group signals in the ^{1}H NMR in different reactional times, were also evaluated in order to investigate the possible hydrolysis of TEP during the sol-gel conversion process (Table 1). As a result, no significant variation of the stoichiometric ratio was observed during the transformations of the 58S liquid precursors in sol and, finally, in the gel network structure. In other words, there was no consumption of the starting material since TEP remained invariant during all the process (**Entries 1–3**).

According to these results, we also decided to investigate the stability of TEP against hydrolysis in acid conditions, but in the absence of TEOS and Ca(NO$_3$)$_2$ in order to remove all the ethanol generated from TEOS hydrolysis (control experiments - Fig. 1b) and, consequently, allowing to have a better understanding about of the behavior of TEP under the hydrolysis reactional conditions (Fig. 4).

^{1}H NMR spectra confirmed the absence of ethanol for all reactional times studied, while the stoichiometric ratio between methylene groups of citric acid and TEP remained also invariant (Table 1, **Entry 4**). Therefore, it can be concluded that acid-catalyzed hydrolysis of TEP does not occur during the investigated time period or even increasing the temperature to 50 °C and a longer reactional time T$_3$ (72 h). This result suggests that TEP hydrolysis should have a high energy barrier, making it unfeasible or even preventing it from occurring under the

Table 1
Data extracted from the spectra of ^{1}H NMR performed to monitor the behavior of the triethyl phosphate within the reaction medium during the evolution from sol towards the gel in the synthesis of 58S and for control experiments.

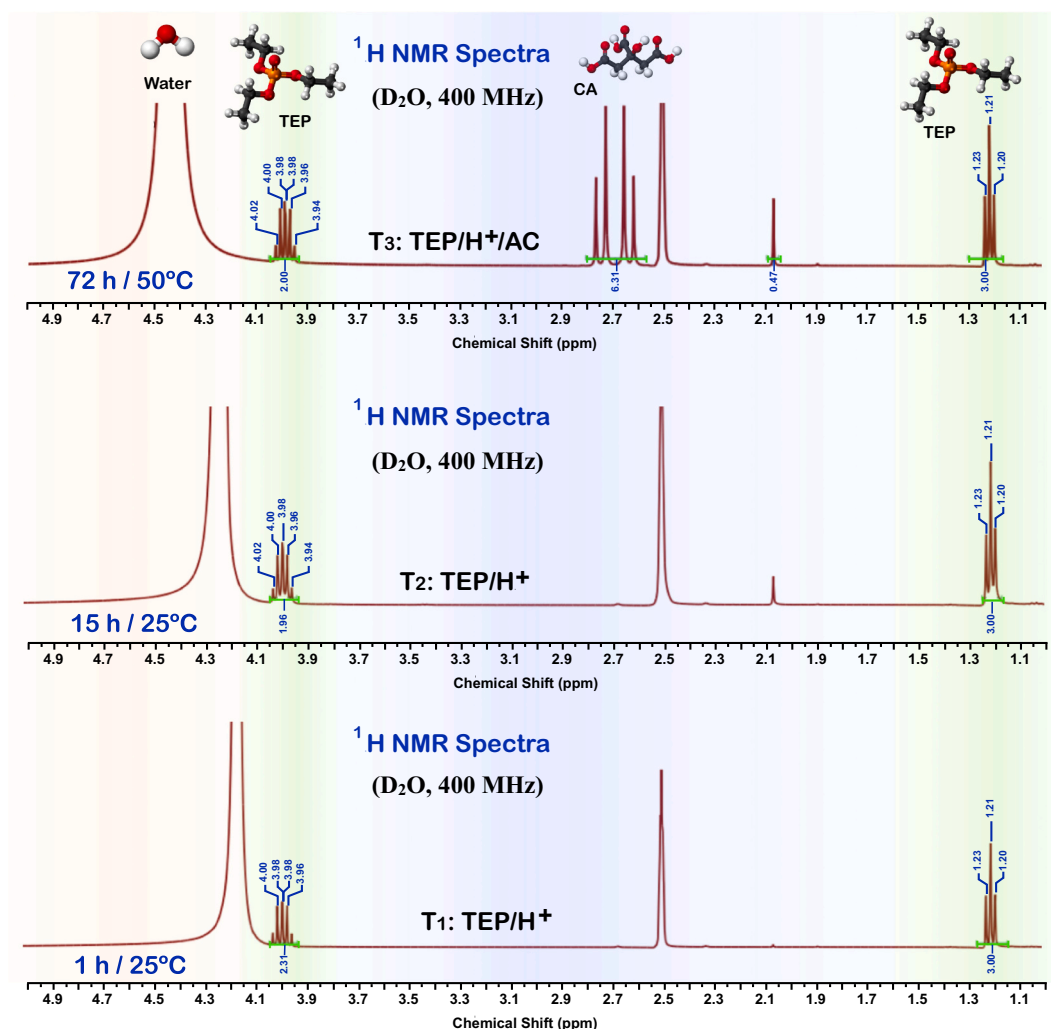| Experiment	Sample	Integral line			Time	Experimental stoichiometric ratio	Theorical stochiometric ratio
		TEP		CA			
		-CH3	-CH2-	-CH2-			
(a)	58S	3.1	2	5.56	T$_1$	0.239	0.22
		3.1	2	5.56	T$_2$	0.239	0.22
		3.1	2	5.38	T$_3$	0.247	0.22
(b)	Control experiments	3.0	2	6.37	T$_3$	0.209	0.22

Fig. 4. ¹H NMR spectrum (D₂O, 400 MHz) for control experiments without TEOS and calcium nitrate. TEP/H⁺ solution for (a) T₁–1 h at 25 °C, (b) T₂–15 h at 25 °C, and (c) TEP/H⁺/CA solution for T₃–72 h at 50 °C.
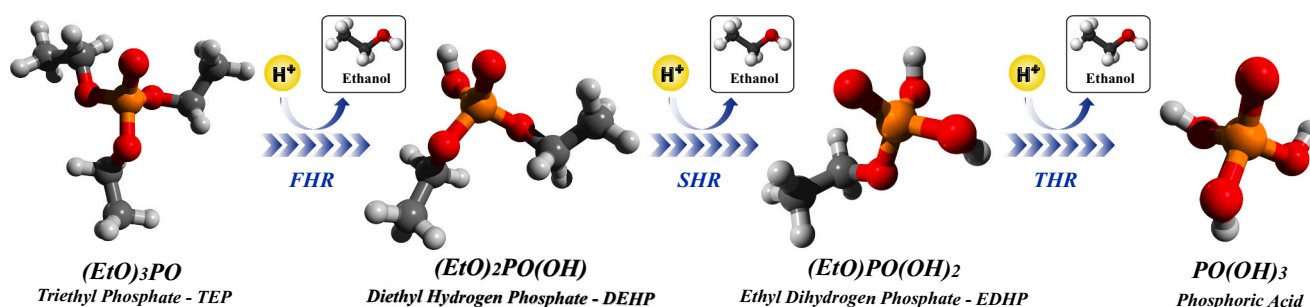

Fig. 5. Schematic representation of the different chemical structures of the alkyl phosphate esters associated with each hydrolysis reaction stage, with phosphoric acid as the final product. The first, second, and third hydrolysis reactions will be referred to as FHR, SHR, and THR, respectively.

investigated conditions. However, its occurrence in the literature has been widely assumed under conditions similar to those studied in the present work. [13,27,33,48] Computational studies were performed aiming to complement and gain more information about the kinetics associated with neutral media and acid-catalyzed triethyl phosphate hydrolysis.

3.2. Density functional theory results

The kinetic behavior was investigated from ab initio DFT calculations by using different categories of models (**C1**: gas phase, **C2**: continuum solvation, and **C3**: mixed solvation). Two types of systems were defined for each category consisting of non-protonated and protonated systems, aiming to represent neutral and acidic systems, respectively. In the **C1** category, the systems are in the gas phase: **S1** (1TEP + 1H₂O) and **S2** (1TEP + 1H₂O + 1H⁺). In the **C2** category, a system similar to the

Table 2
The reaction rates for each stage of TEP hydrolysis (k_{FHR}, k_{SHR} and k_{THR}) and activation energies ($\Delta G^{\ddagger}_{FHR}$, $\Delta G^{\ddagger}_{SHR}$ and $\Delta G^{\ddagger}_{THR}$) obtained at 25 °C for the different categories of models.

Systems		Energy of activation (kcal·mol^{-1})			Rate of reaction (s^{-1})		
Category	Type	$\Delta G^{\ddagger}_{FHR}$	$\Delta G^{\ddagger}_{SHR}$	$\Delta G^{\ddagger}_{THR}$	k_{FHR}	k_{SHR}	k_{THR}
C1	**S1**: 1TEP + 1H$_2$O	53.33	52.48	51.77	5.4×10^{-27}	2.3×10^{-26}	8.0×10^{-26}
	S2: 1TEP + 1H$_2$O + 1H$^+$	23.28	21.81	18.97	5.8×10^{-5}	6.9×10^{-4}	8.4×10^{-2}
C2	**S3**: 1TEP + 1H$_2$O + PCM	35.89	35.69	34.92	3.6×10^{-14}	5.1×10^{-14}	1.8×10^{-13}
	S4: 1TEP + 1H$_2$O + 1H$^+$+PCM	21.11	20.68	19.38	2.4×10^{-3}	4.9×10^{-3}	4.4×10^{-2}
C3	**S5**: 1TEP + 8H$_2$O + PCM	28.45	28.93	29.21	1.9×10^{-9}	4.7×10^{-9}	2.9×10^{-9}
	S6: 1TEP + 8H$_2$O + H$^+$+PCM	20.48	20.52	20.91	7.0×10^{-3}	6.8×10^{-3}	3.5×10^{-3}

previous one was defined, but differentiated by the use of a PCM solvent model: **S3** (1TEP + 1H$_2$O + PCM) and **S4** (1TEP + 1H$_2$O + 1H$^+$ + PCM). Finally, in the **C3** category, several water molecules are explicitly added along with the PCM solvent model: **S5** (1TEP + 8H$_2$O + PCM) and **S6** (1TEP + 8H$_2$O + 1H$^+$ + PCM).

The hydrolysis of triethyl phosphate is a multistage process related to the hydrolysis of various reactive forms of mono, di-, and tri-esters, whose final product is phosphoric acid (Fig. 5).

Table 2 shows the $\Delta G^{\ddagger}$ activation energy barrier obtained from the potential energy curve along the IRC path and the reaction rates for each stage of TEP hydrolysis (k_{FHR}, k_{SHR} and k_{THR}) for all systems defined above. In all cases, the three TEP hydrolysis reaction stages were studied.

The three model categories show different kinetic behaviors for protonated and non-protonated systems. In the category **C1**, the non-protonated system (**S1**) shows activation energy barriers ($\Delta G^{\ddagger}$) around 52 kcal·mol^{-1} for the three stages of TEP hydrolysis (Table 2 - *FHR*, *SHR*, and *THR*). The height of these activation energies at this calculation level makes it clear that the hydrolysis of TEP is hindered. In fact, the kinetic constant for the third hydrolysis reaction ($\Delta G^{\ddagger}_{THR}$) is 8.0×10^{-26} s^{-1}.

In the case of the **S2** system, $\Delta G^{\ddagger}$ shows a height of about 20 kcal·mol^{-1} for the three stages of hydrolysis. This fact indicates that the presence of the proton (H$^+$) near the O=P- group radically accelerates the process-kinetics. On average, when protonating the system, $\Delta G^{\ddagger}$ decreases by approximately 33 kcal·mol^{-1} in any of its three hydrolysis stages. Fig. 6a shows the kinetic behavior for the *THR* stage.

In the **C2** category (continuum solvation models, S3 and S4 systems, Fig. 6b), in the three hydrolysis stages, the same behavior is observed. It can be seen that $\Delta G^{\ddagger}$ of the non-protonated system (**S3**) decreases considerably ($\Delta G^{\ddagger}_{THR}$ = 34.9 kcal·mol^{-1}) compared to **S1** system. This result shows that the PCM solvent causes the same behavior that the proton causes near the O=P- group, both strongly decrease the activation barrier ($\Delta G^{\ddagger}$). Therefore, the interactions of the O=P- group with its environment leaves it susceptible to abrupt changes in its kinetic behavior. In the case of the protonated system (**S4**), $\Delta G^{\ddagger}$ remains almost unmodified ($\Delta G^{\ddagger}_{THR}$ = 19.5 kcal·mol^{-1}) compared to its gas phase system (**S2**). This shows that when the O=P- group is already protonated, the effect of the solvent becomes negligible, presenting a $\Delta G^{\ddagger}$ similar to its protonated gas phase (**S2**).

Furthermore, this model shows that the protonated system decreases its activation energy barrier by approximately 15 kcal·mol^{-1} concerning its non-protonated system in the three hydrolysis stages. By comparing the kinetics of non-protonated (**S3**) and protonated (**S4**) systems, the $\Delta G^{\ddagger}_{THR}$ decreases by 15.5 kcal·mol^{-1} for **S4** (Fig. 6b). Moreover, the catalytic effect of the proton in the gas phase is more dominating than in solvated systems (PCM model). Although $\Delta G^{\ddagger}$ decreases considerably when protonating the system, it is still a high barrier to allow rapid reaction, and higher yet for observing the three stages of hydrolysis in a short time. This characteristic justifies the absence of signals related to ethanol, as a byproduct of TEP hydrolysis, in the preparation of 58S, and also in the kinetic study by NMR.

However, despite being an adequate model for predicting kinetic

behavior, as suggested by Ryu et al. [42], the problems of not considering some explicit solvent molecules are evident. For example, when analyzing the energy profile along with the IRC for the **S3** system (Fig. 6b), an endothermic behavior is seen. This feature arises due to the lack of proton transfer between the solvent and the TEP since solvent molecules are not explicitly considered. To overcome the problem, some explicit solvent molecules were included within the systems as suggested by Ryu et al. [42] and Kamerlin et al. [43] Therefore, a mixed solvation model category **C3** was used to analyze the kinetic behavior of TEP and to compare it with the continuum model already described.

In the **C3** category (**S5** and **S6** systems), the protonated and non-protonated systems show $\Delta G^{\ddagger}$ of approximately 20 and 28 kcal·mol^{-1} in the three stages, respectively. For THR, the kinetic behavior of protonated and non-protonated systems (Fig. 6c) shows $\Delta G^{\ddagger}_{THR}$ of 20.9 and 29.2 kcal·mol^{-1}, respectively. Therefore, this model shows that the protonated system decreases its activation energy barrier by approximately 10 kcal·mol^{-1} concerning its non-protonated system, in its three hydrolysis stages. This result indicates that both models (continuum and mixed solvation) predict a different decrease in the activation energy barrier when a system is protonated and also different barrier height for non-protonated systems. When comparing the systems of categories **C2** and **C3** (continuum solvation and mixed solvation models) a kinetic behavior is observed similar to that predicted by Ryu et al. [42] and Kamerlin et al. [43]. That is, the mixed solvation model predicts a slightly smaller $\Delta G^{\ddagger}$ than the continuum solvation model. However, this occurs only for the non-protonated system, whereas for protonated systems no difference between the two models can be detected. This result suggests that when studying the kinetic behavior of neutral systems, both models show different results. However, for protonated systems, both models predict similar results. In any case, both models show that for the complete TEP hydrolysis, high $\Delta G^{\ddagger}$ values are always observed preventing rapid reaction kinetics. Those high $\Delta G^{\ddagger}$ values imply that these reactions, despite being catalyzed, occur with slow kinetics.

Furthermore, the reaction rates of the non-protonated and protonated systems (**C3** category, **S5** and **S6** systems), in the three hydrolysis reaction stages, were calculated considering the Wigner tunneling approach and zero-point energy (ZPE) correction (Table 2). For the non-protonated systems (**S5**), the rates of reaction in their three consecutive hydrolysis stages are $k_{FHR} = 1.9 \times 10^{-9} s^{-1}$, $k_{SHR} = 4.7 \times 10^{-9} s^{-1}$, and $k_{THR} = 2.9 \times 10^{-9} s^{-1}$. For protonated systems (**S6**) the rates are $k_{FHR} = 7.0 \times 10^{-3} s^{-1}$, $k_{SHR} = 6.8 \times 10^{-3} s^{-1}$, and $k_{THR} = 3.5 \times 10^{-3} s^{-1}$. By comparing our results with experimental values from the literature for non-protonated systems, it is possible to notice a reasonable agreement. Lyznicki et al. [48] reported a rate of reaction of $k_{FHR} = 2.4 x 10^{-9} s^{-1}$ at 25.0 °C for the first stage of hydrolysis.

It is also important to highlight the strong dependence of reaction rates on the temperature. For the FHR in neutral solution, some reported calculated values at different temperatures were: $k_{FHR} = 1.3 x 10^{-6} s^{-1}$ at 79.6 °C [48], $k_{FHR} = 1.6 x 10^{-6} s^{-1}$ at 82.0 °C [46] and for a $k_{FHR} = 8.3 x 10^{-6} s^{-1}$ at 101.0 °C [48]. Also, for the last hydrolysis stage the value of $k_{THR} = 7.0 x 10^{-7} s^{-1}$ at 100.0 °C has been reported for neutral solution [47]. These reaction rate values suggest that apparently a temperature
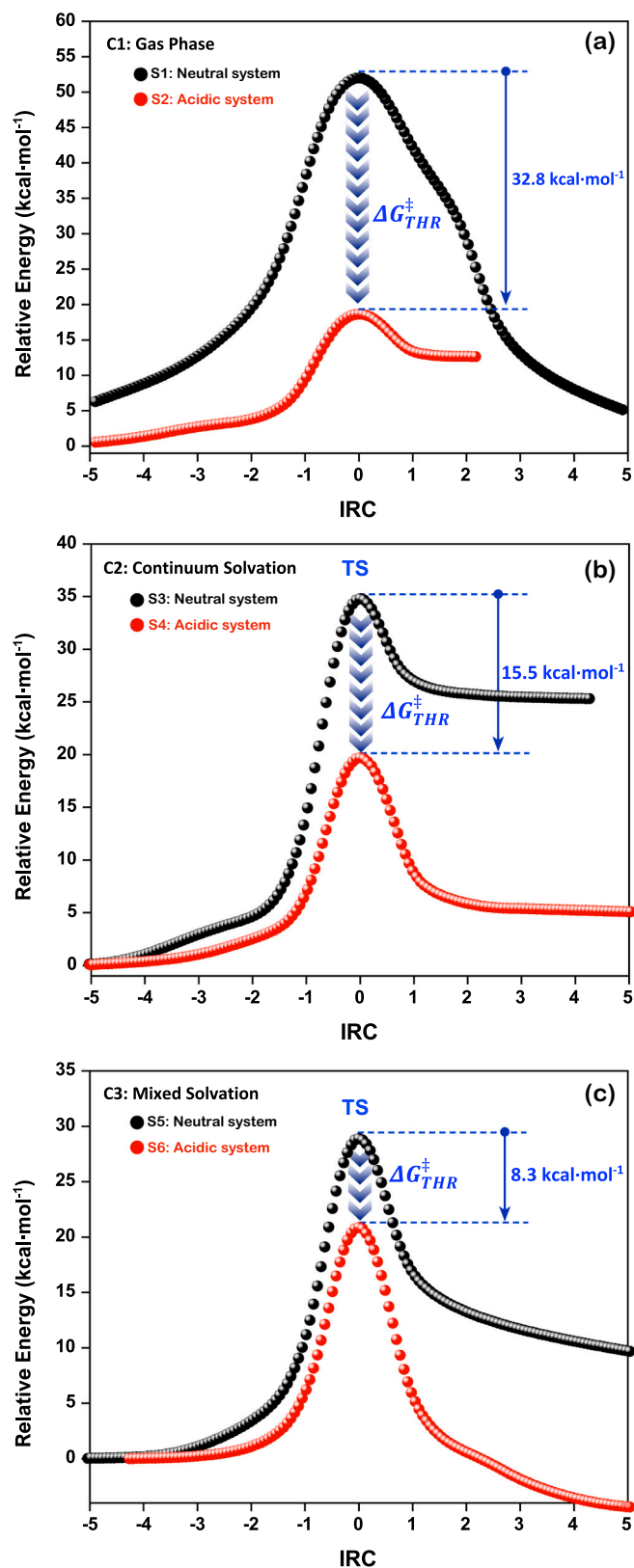
Fig. 6. Energy profile along IRC for non-protonated (black curve) and protonated (red curve) systems for the three TEP hydrolysis reactions. (a) C1 category - S1: (1TEP + 1H$_2$O) and S2: (1TEP + 1H$_2$O + 1H$^+$). (b) C2 category - S3: (1TEP + 1H$_2$O + PCM) and S4: (1TEP + 1H$_2$O + 1H$^+$ + PCM). (c) C3 category - S5: (1TEP + 8H$_2$O + PCM) and S6: (1TEP + 8H$_2$O + 1H$^+$ + PCM). (For interpretation of the references to colour in this figure legend, the reader is referred to the web version of this article.)
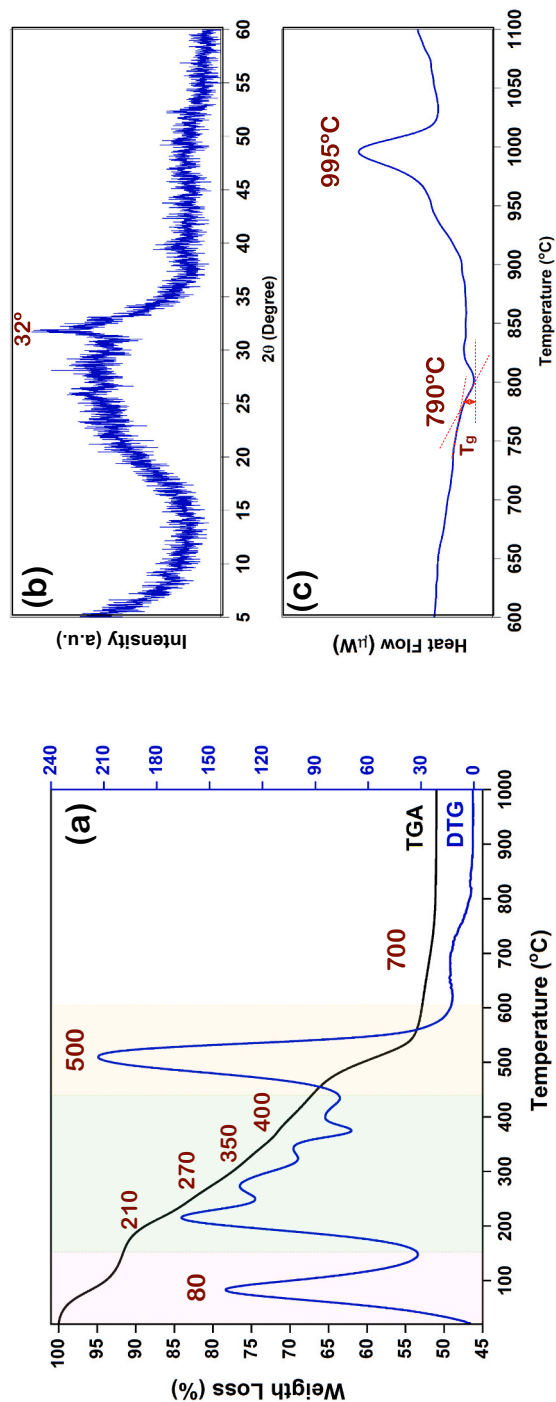

Fig. 7. (a) TGA curve for 58S xerogels and its respective DTG derivative. Based on the results of the thermogravimetric analysis, the xerogel calcination temperature was set at 600 °C. Thus, prior to XRD and DSC analyses, the XG58S was calcined at 600 °C for 12 h aiming to remove all organic load and consolidate the vitreous structure. (b) X-ray diffraction pattern and (c) DSC curve for 58S after calcination step.
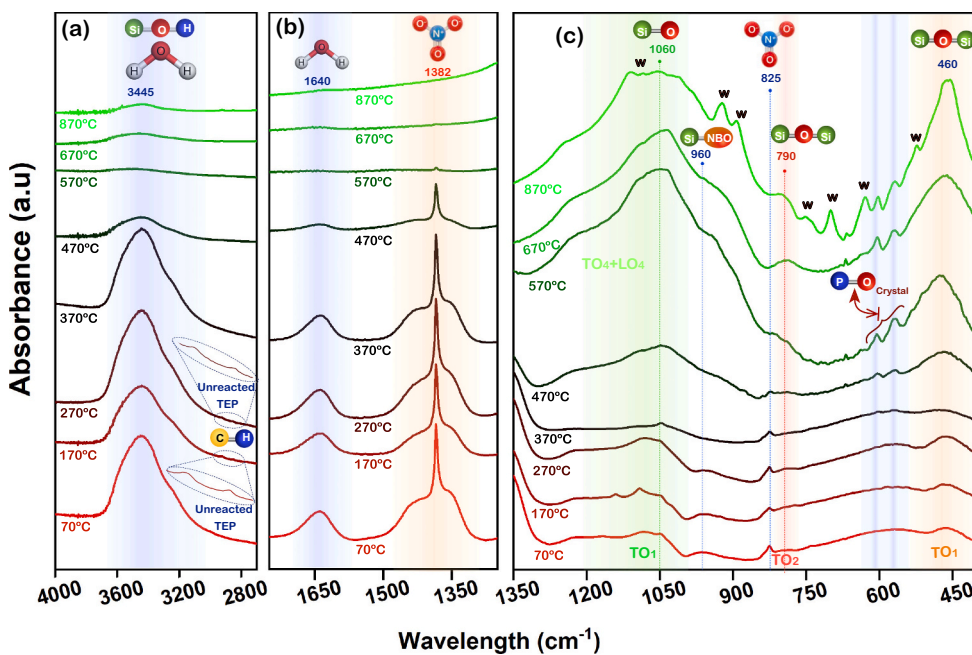
Fig. 8. Structural evolution for xerogel as a function of calcination temperature monitored by infrared spectroscopy (FTIR). The presence of unreacted TEP can be clearly seen in the zoomed region around the C—H absorption for xerogel thermal treated up to 270 °C (*Panel - a*). Water and nitrate species were continuously removed from xerogel as the calcination temperature is increased (*Panel - b*). The complex absorption band in the region of 900–1200 cm^{-1} is assigned to the overlap of the Si—O, P—O and P$\equiv$O stretching vibrations. This absorption has its intensity increased and becomes more defined for heat treatments at higher temperatures. Moreover, the emergence of the doublet in the region of 550–650 cm^{-1} characteristic of the phosphorus-rich crystalline phase, is clearly noticeable at temperatures above 370 °C (*Panel - c*). The devitrification process is evident at temperatures above 870 °C with the emergence of typical narrow bands assigned to the wollastonite (w), which is the crystalline phase commonly formed in 58S glass subjected to heat treatment.

increase up to 79.6 °C accelerates hydrolysis more effectively than higher temperatures. In addition, the results on the effect of the counterion (SO_4^{-1} and ClO_4^{-1}) on the hydrolysis kinetics were also shown to be important. Bel'skii [47] reported that under acid condition ($HClO_4$, 4 M) the kinetic constant is $k_{THR} = 9.9 \times 10^{-6} s^{-1}$ at 100 °C, whereas in neutral solution the $k_{THR} = 7.0 \times 10^{-7} s^{-1}$ at the same temperature. These results show that the effect of the counterion can be important, but it also makes it clear that the TEP hydrolysis reaction kinetics in protonated systems is still very slow.

Regarding the kinetic behavior of the systems in which the continuous solvation model was used (category **C2**), high $\Delta G^{\ddagger}$ are observed. Consequently, the calculated kinetic constants are even lower compared to those obtained for the mixed solvation model. Indeed, the predicted values for the reaction rate constants predicted by the continuum solvation models are much lower and would not be experimentally realistic. The main conclusion that can be drawn from these kinetic data is that regardless of the model used, all results show low values for the reaction rates for each stage of triethyl phosphate hydrolysis (k_{FHR}, k_{SHR} and k_{THR}), which is characteristic of reactions with slow kinetics. Thus, the hydrolysis of TEP would not be expected in the time scale involved, in the reaction time studied, or in the sol-gel synthesis of 58S bioactive glass.

3.3. Structural evolution in response to calcination temperature: from gel to bioactive glass formation 58S

No precipitate formation was observed in the resulting sol derived from the combination of NFS and NMS precursor solutions, the sol remaining transparent throughout the evolution from sol to gel phase. In the post-aging stage, the gel was converted to xerogel by drying in an oven at 50 °C for 3 days (Fig. 1c). The main thermal events associated with xerogel thermal evolution and the determination of the ideal calcination temperature were characterized by thermogravimetric analyses (Fig. 7a).

The TGA curve reveals a weight loss of approximately 50% due to the presence of organic load and reaches stabilization at 550 °C. The DTG curve, up to 150 °C, presents an initial weight loss associated with removal of the residual ethanol produced by the hydrolysis of the TEOS and TEP and water molecules. Another thermal event extends over a wide range from 160 up to 450 °C, corresponding to the overlapping of

the weight loss owing to the ethyl groups present in the precursors TEOS and TEP, vaporization of unhydrolyzed triethyl phosphate (~215 °C), ethanol (residual hydrolysis by-product), condensation of vicinal OH groups and geminal OH groups present on the xerogel surface. The most intense thermal event around 30% at 500 °C is associated with the decomposition of nitrate groups. The small and broad peak can be observed at higher temperature is related to the condensation of free hydroxyl groups on the silica surface [13].

Based on xerogel thermogravimetry data it is possible to infer that all the organic charge has been removed from the matrix and a possible glass structure has been established at 600 °C. The long-range ordering in the calcined xerogel at 600 °C was investigated by XRD diffraction (Fig. 7b), which exhibits a small peak near 2θ = 30° emerging from the amorphous halo. This result indicates the coexistence of non-crystalline portions permeating the crystalline domains (glass-ceramic). Indeed, non-crystalline portions manifest through the glass transition phenomenon on the DSC curve (Fig. 7c). The identification of the crystalline phase present in the calcined xerogel may become obscure due to the complexity of the glass composition, considering that the signals concerning the possible crystalline silicate and/or calcium-rich phosphates phases present in poorly ordered environments exhibit overlapping diffraction patterns. Balamurugan et al. [49] report on the structural transformations of 58S bioactive glass during thermal treatments and observed that X-ray diffraction peaks matched the pattern of wollastonite $CaSiO_3$ (JCPDS #27-0088). However, the ray diffractogram presented in Fig. 7b does not match the X-ray diffraction peaks of wollastonite, suggesting the presence of another crystalline phase.

The results obtained by the aforementioned XRD confirm the phase separation in 58S calcined at 600 °C, which is the calcination temperature commonly used in the synthesis of this biomaterial [10,25,50]. The next step is to investigate when this event occurs during the evolution of sol towards the gel phase or in the calcination step, as well as gain insights into the crystalline phase formed. To find the answers to the questions above, a detailed study on the evolution of the short-range order (SRO) as a function of temperature within the atomic structure of xerogel 58S during the calcination step was performed. Important insights into the structural features of the structural transformations of xerogel as a function of calcination temperature were obtained by FTIR (Fig. 8).

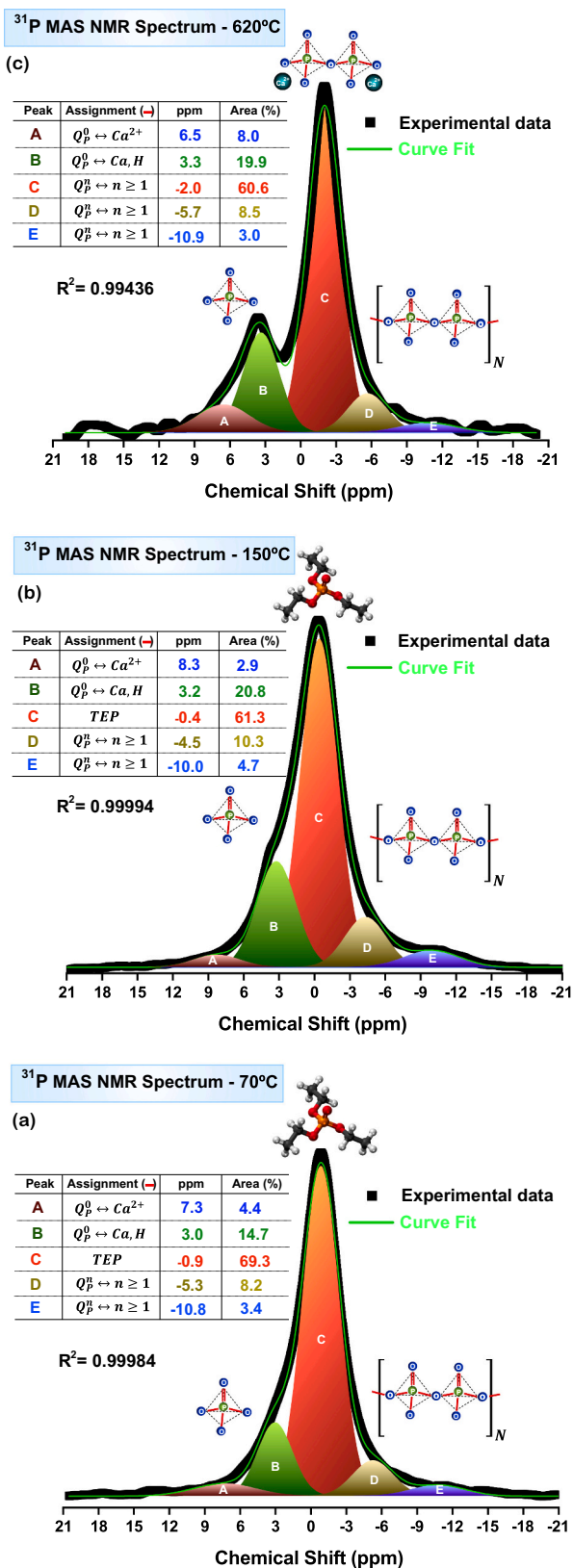The infrared spectrum of xerogel 58S treated at 70 °C preserves the

³¹P MAS NMR Spectrum - 620°C

(c)

Peak	Assignment (↩)	ppm	Area (%)
A	$Q_P^0 \leftrightarrow Ca^{2+}$	6.5	8.0
B	$Q_P^0 \leftrightarrow Ca, H$	3.3	19.9
C	$Q_P^n \leftrightarrow n \geq 1$	-2.0	60.6
D	$Q_P^n \leftrightarrow n \geq 1$	-5.7	8.5
E	$Q_P^n \leftrightarrow n \geq 1$	-10.9	3.0

$R^2 = 0.99436$

■ Experimental data
— Curve Fit

³¹P MAS NMR Spectrum - 150°C

(b)

Peak	Assignment (↩)	ppm	Area (%)
A	$Q_P^0 \leftrightarrow Ca^{2+}$	8.3	2.9
B	$Q_P^0 \leftrightarrow Ca, H$	3.2	20.8
C	TEP	-0.4	61.3
D	$Q_P^n \leftrightarrow n \geq 1$	-4.5	10.3
E	$Q_P^n \leftrightarrow n \geq 1$	-10.0	4.7

$R^2 = 0.99994$

■ Experimental data
— Curve Fit

³¹P MAS NMR Spectrum - 70°C

(a)

Peak	Assignment (↩)	ppm	Area (%)
A	$Q_P^0 \leftrightarrow Ca^{2+}$	7.3	4.4
B	$Q_P^0 \leftrightarrow Ca, H$	3.0	14.7
C	TEP	-0.9	69.3
D	$Q_P^n \leftrightarrow n \geq 1$	-5.3	8.2
E	$Q_P^n \leftrightarrow n \geq 1$	-10.8	3.4

$R^2 = 0.99984$

■ Experimental data
— Curve Fit

Fig. 9. ³¹P MAS NMR spectra for 58S xerogels calcined at (a) 70 °C, (b) 150 °C, and (c) 620 °C. The gyromagnetic constant for ³¹P is positive ($\gamma = 10.841 \times 10^7$ rad·T⁻¹·s⁻¹), the signal related to the polymerized species of phosphorus ($_PQ^1$, $_PQ^2$, $_PQ^3$) is present as negative values of δ (ppm) of ³¹P MAS NMR spectrum.

spectral characteristics of precursors employed in the synthesis of the gel (water, silica, nitrate, etc.). Higher frequencies (3600–3000 cm⁻¹) related to the overtones or combinations of hydrogen-bonded OH stretching (Si-OH or H₂O) [51,52] (Fig. 8a), and the absorption at ~1640 cm⁻¹ related to the deformation mode of undissociated water molecules ($\delta_{\text{H-O-H}}$) [53] (Fig. 8b). As a result, their intensities decrease progressively and practically disappear in the IR spectrum for samples calcined above 470 °C. The nitrate species has a symmetry group D_{3h} and usually manifests through the presence of three vibrational modes $\nu_2(D_{3h}) = 820$ cm⁻¹, $\nu_3(D_{3h}) = 1387$ cm⁻¹ and $\nu_4(D_{3h}) = 750$ cm⁻¹ (Fig. 8b and c) [53,54]. The presence of calcium ions promotes deformation in nitrate trigonal geometry promoting the appearance of other small absorptions due to the symmetry change from D_{3h} to C_{2v} (Fig. 8c) [54]. In full agreement with the TGA data, the absorptions at $\nu_2(D_{3h}) = 820$ cm⁻¹ and $\nu_3(D_{3h}) = 1387$ cm⁻¹ decrease continuously as the xerogel calcination temperature is increased, disappearing for thermal treatments above 570 °C. Silica network formation is observed by the presence of transversal optical (TO) main modes commonly present in all silica-based materials, i.e., rocking (TO₁) (457–507 cm⁻¹), symmetric (TO₂) (810–820 cm⁻¹) and antisymmetric (TO₃) (1070–1250 cm⁻¹) vibrations of oxygen atoms in Si-O-Si bonds with a shoulder around 1220 cm⁻¹ (disorder-induced longitudinal-transverse vibrational mode (($LO_4 - TO_4$))) [27,52,53,55]. The presence of calcium ions induce significant differences in the silicon-oxygen bond vibrations, for instance, the absorption related to the stretching mode preserves its frequency and becomes broader with maximum intensity around $\nu_{(Si-O)} = 1055$ cm⁻¹, whereas bending ($\nu_{(Si-O-Si)} = 760$ cm⁻¹) and rocking ($\nu_{(O-Si-O)} = 480$ cm⁻¹) modes, besides widening, display a vibration energy at lower wavelengths (Fig. 8c) [27,52,53]. Such events can be observed for the calcined sample from 470 °C when calcium ions begin to break the silicate network ($Si - O - Si \to Si - O^- Ca^{2+} O^- - Si$) after nitrate degradation [52].

The evolution in the chemical environment of phosphorus during calcination can be accompanied by the $\delta_{(O-P-O)}$ vibrational mode in the region of 550–610 cm⁻¹ [53]. The IR spectra for calcined xerogel from 370 °C show the appearance of two small peaks at 565 and 603 cm⁻¹ that have their intensities increased to higher temperatures becoming quite clear at 570 °C. The presence of this well-defined doublet in the spectrum indicates the presence of P—O in the crystal, indicating the onset of a phase separation and the formation of phosphorus-rich crystalline domains [27,52,53]. The absence of the doublet in the IR spectrum of the xerogel treated up to 270 °C may be related to the presence of unhydrolyzed TEP or/and P—O in the formation of amorphous phosphorus species (ortho- $_PQ^0$, pyro- $_PQ^1$ or meta- $_PQ^2$). IR spectra show a strong evidence of the non-hydrolysis of TEP manifested by the non-disappearance of the subtle absorptions in the 2800–3000 cm⁻¹ range attributed to the symmetric and asymmetric stretching vibrational modes of the ethyl groups (C—H bonds) (see the zoomed region in Fig. 8a) [55]. The absence of absorptions related to C—H bonds would confirm the successful hydrolysis of triethyl phosphate since neither TEOS (fast hydrolysis reaction kinetics) or ethanol (high vapor pressure) should no longer be present in the reaction medium. Indeed, ³¹P MAS NMR spectra clearly show that TEP remains non-hydrolyzed until 150 °C when the presence of ortho- and polyphosphate species can be noticed (Fig. 9).

Recognizing the greater strength of P-O-P and/or Si-O-Si bonds than Si-O-P and the higher stability of P-O-Ca bonds compared to Si-O-Ca bonds as well as the low P concentration in the glass composition, the crystal-type environment for phosphorus is consistent with the presence of calcium orthophosphate ($_PQ^0$) and/or calcium pyrophosphate ($_PQ^1$) within the glass matrix [56]. However, the discernment between ortho- or polyphosphate species by FTIR in the vitreous matrix may become obscure due to the superposition of the signals referring to the vibrational modes of phosphorus by the silicon species, which is present in higher concentration.

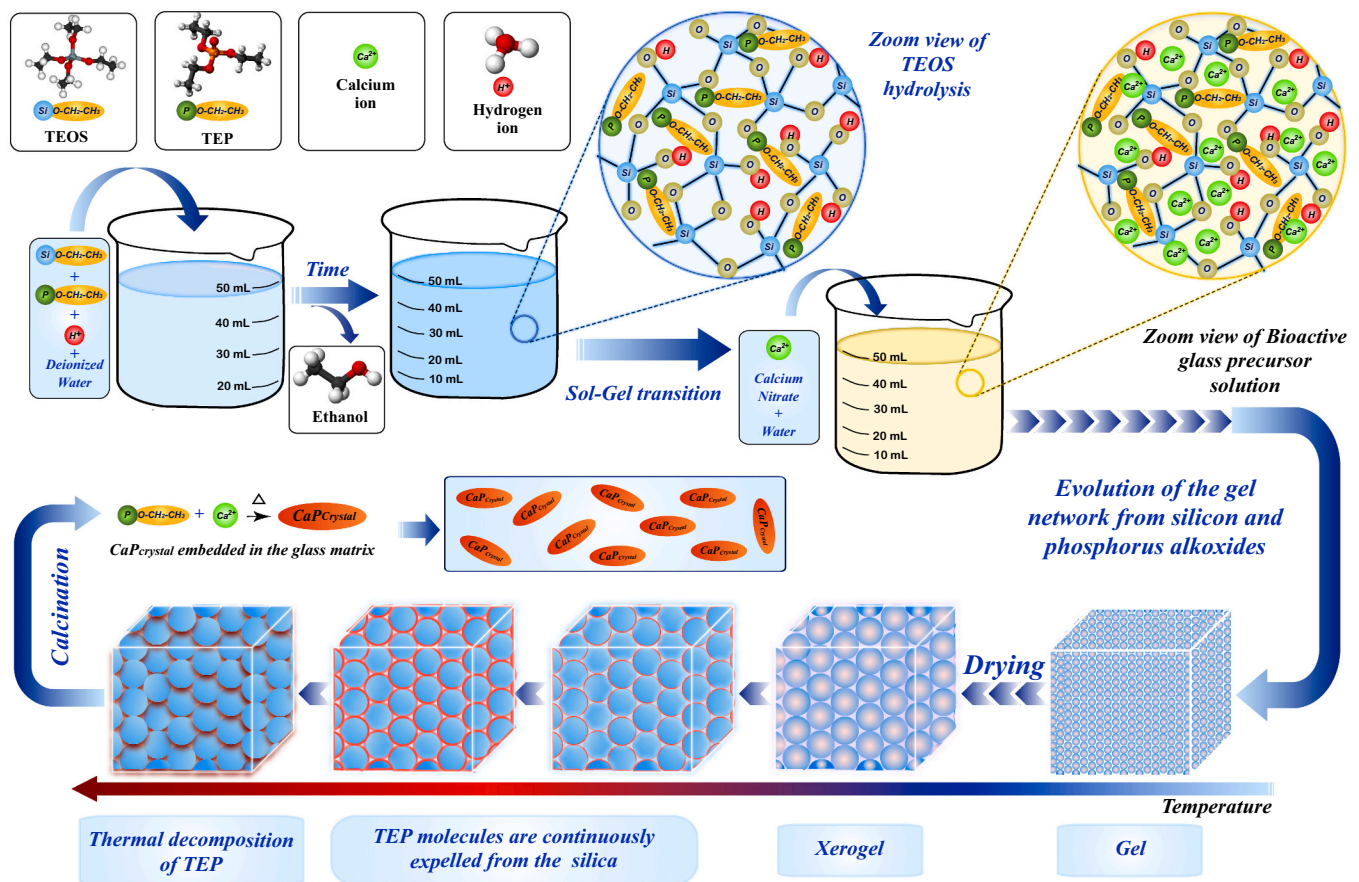Unlike other analysis methods, MAS NMR spectroscopy is a

Fig. 10. Scheme illustrating the mechanism related to the events that occur during the evolution of the sol towards the gel phase and calcination step that lead to phase separation in 58S bioactive glass obtained via the sol-gel route.

powerful, univocal, and sensitive tool for investigating the chemical environment of phosphorus. ^{31}P MAS NMR spectrum of the xerogel calcined at 620 °C (calcination temperature commonly used for 58S) shows a curve profile and isotropic chemical changes for phosphate sites consistent with the presence of crystalline calcium pyrophosphate as the major phase and a small fraction of calcium orthophosphate (Fig. 9c) [13]. It is important to note that the ortho- and polyphosphate species are already present since the xerogel phase (Fig. 9a). Furthermore, the quantity of Q_P^0 species remains unchanged throughout the calcination step, while polymerized phosphorus content increased considerably after the thermal decomposition of triethyl phosphate into $Q_P^{n \geq 1}$ species (Fig. 9a–c). The formation of crystalline calcium pyrophosphates and/or other polyphosphate species has an inhibitory effect on biomineralization due to the consequent immobilizations of soluble ions in the material matrix [56,57]. In other words, the NMR data corroborated the proposed chemical model to explain the behavior of TEP during 58S bioactive glass synthesis, which predicts that ester bonds (P-O-C) are broken only in the calcination step.

3.4. Model for phase separation in 58S synthesis

The bioactive glass was developed in the 1960s and since then it has attracted considerable attention for its ability to interact with living tissues and the ability to stimulate regeneration of damaged tissues. The action of bioactive glass is based on its ability to deliver controlled and localized species with biological importance - ion therapy. These species present at critical concentrations up-regulate gene families important for bone regeneration. In this sense, the presence of a homogeneous glass structure is extremely important from a bioactivity standpoint. The

presence of heterogeneities in the microstructure of the glass alters the release rates of these species bringing negative effects to bioactivity. In the sol-gel approach, the nature of the alkoxide precursor plays a remarkable role in the synthesis of homogeneous multi-component glass. A possible non-hydrolysis of one of the precursors may lead to the phase separation and formation of agglomerates, which are undesirable in the xerogel.

A schematic representation of the proposed mechanism for phase separation and the formation of crystalline domains in the sol-gel synthesis of bioactive glass based on non-hydrolysis of TEP is presented in Fig. 10.

In our model, TEOS undergoes rapid hydrolysis, followed by immediate condensation leading to the formation of three-dimensional silica gels, that permeate non-hydrolyzed triethyl phosphate molecules due to its slow kinetic rate. In this scenario, TEP does not undergo hydrolysis reaction during the formation of silica particles (precursor of the silica backbone) in the sol or the gel phase until its thermal decomposition in the calcination step. During the silica particle growth process, TEP molecules are continuously expelled from the newly formed matrix rich in silica, concentrating on the surface/interstitials of the particles. In this scenario, TEP continually accumulates at the edges of the particles as the silica backbone forms, creating domains rich in unhydrolyzed triethyl phosphate (see *FTIR* and ^{31}*P MAS NMR discussion*). At this stage, the mobility of phosphate species by the matrix is considerably lower than in the sol or gel phase. During the calcination step, the TEP undergoes thermal decomposition around 250 °C (see ***TGA discussion***) when it is preferentially associated with the more labile species, in this case, the calcium ions present in its vicinity, forming small crystalline domains permeated by the silica-rich glass matrix. Consequently, the proximity of

phosphorus species confined in domains leads to the formation of polyphosphates such as calcium pyrophosphates, among others. These phosphate species are characterized by low solubility and are often associated with the bioinactivation of glass with bioactive compositions [26,56,57]. Furthermore, the presence of crystalline calcium pyrophosphate domains embedded within the vitreous matrix (heterogeneities) modifies the resulting vitreous composition and drastically modifies the chemical composition, structure, and consequently, other important properties that are closely related to bioactivity [9,13,58].

Another challenge associated with the presence of triethyl phosphate in the non-hydrolyzed form in the gel/xerogel would be the fine control of the chemical composition of the prepared bioactive glass. The boiling point of triethyl phosphate is 215 °C [59], consequently, a partial loss of this alkoxide by vaporization becomes inevitable during the calcination step of the xerogel. This effect becomes quite pronounced since most of the TEP molecules accumulate on the surface and in the interstices of the silica nanoparticles during the growth of the silicate domains in the xerogel matrix. Indeed, the thermogravimetric analysis of the 58S precursor xerogel shows an intense mass loss at 215 °C, possibly related to the vaporization of part of the TEP molecules from the xerogel.

Any progress in this field requires a method of synthesis that favors an improved microstructure (high structural homogeneity) and also that allows fine control of the chemical composition of prepared glass. In our previous work, we reported an efficient strategy for the synthesis of 58S bioactive glass with high structural homogeneity and accurate chemical composition through the citric acid assisted sol-gel route coupled to the self-propagating combustion method (SPC). Indeed, several studies have shown that bioactive glass obtained through the "citrate sol-gel" method exhibit an improved microstructure, which directly impacts the solubility and the rate of HCA formation. It is worth mentioning that critical concentrations of ionic dissolution products (Si, Ca, and P species) released from bioactive glass can stimulate the genes of cells towards a path of regeneration and repair of living tissues. Thus, the results reported in the present study reinforce the importance of understanding the mechanisms involved in the sol-gel synthesis for obtaining glasses with differentiated microstructural characteristics.

4. Conclusions

We investigated the mechanism associated with phase separation and the formation of crystalline phases during the synthesis of 58S bioactive glass. NMR results showed that the hydrolysis reaction of TEP does not occur in the time scale involved in the sol-gel synthesis of 58S bioactive glass. DFT results revealed that for any TEP hydrolysis stage, the reaction occurs at a very slow kinetics rate, even under excess proton conditions (acid systems). Therefore, for short reaction times, as in the case of the 58S precursor solution, it is expected that not even the first hydrolysis reaction of the TEP will be observed.

The study on the evolution of the short-range ordering within the atomic structure of xerogel 58S during the calcination step showed that the silica network formed in the gelation stage contains unreacted TEP species dispersed into the gel. In the calcination step, the thermal decomposition of TEP occurs around 250 °C, when the P preferentially associates with labile and vicinity species forming small crystalline calcium pyrophosphate domains permeated by the silica-rich glass matrix. It is worth emphasizing that the short and medium-range structures of the bioactive glass describe the way cations are arranged around the silicate and phosphate species, which in turn affects their energetics and rates of breaking off and releasing these ions/species into solution. Thus, understanding and controlling the microstructure of glass are key factors from the viewpoint of glass dissolution (dissolution rate) and have a profound influence on the early events, which are crucial on the subsequent reactions on the glass surface, and consequently the bioactivity of the biomaterial. Our findings are very important in order to understand the molecular mechanisms involved in sol-gel processes for the preparation of bioactive glass with high structural homogeneity.

Author contributions

O. M. V. M. Bueno, M. A. San-Miguel, and J. H. Lopes conceived and performed the experiments, analyzed the results, and wrote the paper. C. L. Herrera and J. H. Lopes performed the spectroscopic observation. All authors reviewed the paper.

Declaration of competing interest

The authors declare no competing financial interests.

Appendix A. Supplementary data

Supplementary data to this article can be found online at https://doi.org/10.1016/j.msec.2020.111759.

References

[1] R.H. Doremus, Glass Science, Wiley, 1994.
[2] O.L. Alves, I.F. Gimenez, I.O. Mazali, Cadernos temáticos - Química Nova na Escola, Maio (2001) 13–24.
[3] K.J. Rao, Chapter 3 - the Glass Transition Phenomenon, Structural Chemistry of Glasses, Elsevier Science Ltd, Oxford, 2002, pp. 77–135.
[4] P.K. Gupta, J. Non-Cryst. Solids 195 (1996) 158–164.
[5] J.E. Shelby, Structures of glasses, in: J.E. Shelby (Ed.), Introduction to Glass Science and Technology, The Royal Society of Chemistry, 2007, pp. 72–110.
[6] J.E. Shelby, Immiscibility/phase separation, in: J.E. Shelby (Ed.), Introduction to Glass Science and Technology, The Royal Society of Chemistry, 2007, pp. 51–71.
[7] M. Brink, T. Turunen, R.P. Happonen, A. Yli-Urpo, J. Biomed. Mater. Res. 37 (1997) 114–121.
[8] J.H. Lopes, A. Magalhães, I.O. Mazali, C.A. Bertran, H.E. Kim, J. Am. Ceram. Soc. 97 (2014) 3843–3852.
[9] J.H. Lopes, I.O. Mazali, R. Landers, C.A. Bertran, H.E. Kim, J. Am. Ceram. Soc. 96 (2013) 1464–1469.
[10] F.V. Ferreira, L.P. Souza, T.M.M. Martins, J.H. Lopes, B.D. Mattos, M. Mariano, I. F. Pinheiro, T.M. Valverde, S. Livi, J.A. Camilli, A.M. Goes, R.F. Gouveia, L.M. F. Lona, O.J. Rojas, Nanoscale 11 (2019) 19842–19849.
[11] L.P.L. de Souza, J.H. Lopes, F.V. Ferreira, R.A. Martin, C.A. Bertran, J.A. Camilli, Evaluation of effectiveness of 45S5 bioglass doped with niobium for repairing critical-sized bone defect in in vitro and in vivo models, J Biomed Mater Res A 108 (3) (2020) 446–457, https://doi.org/10.1002/jbm.a.36826. Epub 2019 Nov 7. PMID: 31657517.
[12] J.R. Jones, Sol-Gel Derived Glasses for Medicine, Bio-Glasses, John Wiley & Sons, Ltd, 2012, pp. 29–44.
[13] J.H. Lopes, O. Bueno, I.O. Mazali, C.A. Bertran, Mater. Sci. Eng. C Mater. Biol. Appl. 97 (2019) 669–678.
[14] S.P. Mukherjee, J. Non-Cryst. Solids 42 (1980) 477–488.
[15] S. Sakka, Sol–gel formation of bulk glasses, in: L. Klein, M. Aparicio, A. Jitianu (Eds.), Handbook of Sol-Gel Science and Technology, Springer International Publishing, Cham, 2017, pp. 1–24.
[16] J. Chen, L. Zeng, X. Chen, T. Liao, J. Zheng, Bioactive Materials 3 (2018) 315–321.
[17] A.E. Danks, S.R. Hall, Z. Schnepp, Mater Horiz 3 (2016) 91–112.
[18] H. Luo, W. Li, H. Ao, G. Li, J. Tu, G. Xiong, Y. Zhu, Y. Wan, Mater. Sci. Eng. C 76 (2017) 94–101.
[19] A. Moghanian, A. Sedghi, A. Ghorbanoghli, E. Salari, Ceram. Int. 44 (2018) 9422–9432.
[20] H. Luo, Y. Zhang, Z. Wang, Z. Yang, J. Tu, Z. Liu, F. Yao, G. Xiong, Y. Wan, Chem. Eng. J. 326 (2017) 210–221.
[21] K. Maji, S. Dasgupta, K. Pramanik, A. Bissoyi, International Journal of Biomaterials 2016 (2016) 14.
[22] S. Hattar, S. Loty, D. Gaisser, A. Berdal, J.M. Sautier, J. Biomed. Mater. Res. A 76 (2006) 811–819.
[23] P. Sepulveda, J.R. Jones, L.L. Hench, J. Biomed. Mater. Res. 61 (2002) 301–311.
[24] W. Gong, Y. Dong, S. Wang, X. Gao, X. Chen, RSC Adv. 7 (2017) 13760–13767.
[25] W.Y. Gong, Y.M. Dong, X.F. Chen, B. Karabucak, Chin J Dent Res 15 (2012) 145–152.
[26] A. Tilocca, A.N. Cormack, N.H. de Leeuw, Faraday Discuss. 136 (2007) 45–55 (discussion 107-123).
[27] R.L. Siqueira, E.D. Zanotto, J Mater Sci Mater Med 24 (2013) 365–379.

[28] S. Ni, R. Du, S. Ni, Adv. Mater. Sci. Eng. 2012 (2012) 1–7.
[29] C. Gao, T. Liu, C. Shuai, S. Peng, Sci. Rep. 4 (2014) 4712.
[30] X. Kesse, C. Vichery, J.M. Nedelec, ACS Omega 4 (2019) 5768–5775.
[31] A. Tilocca, A.N. Cormack, J. Phys. Chem. C 112 (2008) 11936–11945.
[32] S.H. Hilal, U.S. Environmental Protection Agency, Office of Research and Development, Washington, DC, 2006, pp. 11–12.
[33] J.R. Jones, Sol-gel materials for biomedical applications, in: D. Levy, M. Zayat (Eds.), The Sol-Gel Handbook, 2015, pp. 1345–1370.
[34] Y. Zhao, D.G. Truhlar, Accounts Chem Res 41 (2008) 157–167.
[35] Y. Zhao, N.E. Schultz, D.G. Truhlar, J. Chem. Theory Comput. 2 (2006) 364–382.
[36] M.J. Frisch, G.W. Trucks, H.B. Schlegel, G.E. Scuseria, M.A. Robb, J.R. Cheeseman, G. Scalmani, V. Barone, G.A. Petersson, H. Nakatsuji, X. Li, M. Caricato, A.V. Marenich, J. Bloino, B.G. Janesko, R. Gomperts, B. Mennucci, H.P. Hratchian, J.V. Ortiz, A.F. Izmaylov, J.L. Sonnenberg, Williams, F. Ding, F. Lipparini, F. Egidi, J. Goings, B. Peng, A. Petrone, T. Henderson, D. Ranasinghe, V.G. Zakrzewski, J. Gao, N. Rega, G. Zheng, W. Liang, M. Hada, M. Ehara, K. Toyota, R. Fukuda, J. Hasegawa, M. Ishida, T. Nakajima, Y. Honda, O. Kitao, H. Nakai, T. Vreven, K. Throssell, J.A. Montgomery Jr., J.E. Peralta, F. Ogliaro, M.J. Bearpark, J.J. Heyd, E.N. Brothers, K.N. Kudin, V.N. Staroverov, T.A. Keith, R. Kobayashi, J. Normand, K. Raghavachari, A.P. Rendell, J.C. Burant, S.S. Iyengar, J. Tomasi, M. Cossi, J.M. Millam, M. Klene, C. Adamo, R. Cammi, J.W. Ochterski, R.L. Martin, K. Morokuma, O. Farkas, J.B. Foresman, D.J. Fox, Wallingford, CT, 2009.
[37] R. Xiao, M. Noerpel, H. Ling Luk, Z. Wei, R. Spinney, Int. J. Quantum Chem. 114 (2014) 74–83.
[38] R.P. Bell, Trans. Faraday Soc. 55 (1959) 1–4.
[39] J.R. Leon-Carmona, A. Galano, J. Phys. Chem. B 115 (2011) 4538–4546.
[40] J.R. Alvarez-Idaboy, A. Galano, Theor. Chem. Accounts 126 (2009) 75–85.
[41] A. Galano, J.R. Alvarez-Idaboy, J. Comput. Chem. 27 (2006) 1203–1210.

[42] H. Ryu, J. Park, H.K. Kim, J.Y. Park, S.-T. Kim, M.-H. Baik, Organometallics 37 (2018) 3228–3239.
[43] S.C.L. Kamerlin, M. Haranczyk, A. Warshel, ChemPhysChem 10 (2009) 1125–1134.
[44] Y. Dubitsky, A. Zaopo, G. Zannoni, L. Zetta, Mater. Chem. Phys. 64 (2000) 45–53.
[45] J.C. Echeverría, P. Moriones, G. Arzamendi, J.J. Garrido, M.J. Gil, A. Cornejo, V. Martínez-Merino, J Sol-Gel Sci Techn 86 (2018) 316–328.
[46] E.M. Thain, Journal of the Chemical Society (Resumed), 1957, pp. 4694–4699.
[47] V.E. Bel'skii, Russ. Chem. Rev. 46 (1977) 828–841.
[48] E.P. Lyznicki Jr., K. Oyama, T.T. Tidwell, Can. J. Chem. 52 (1974) 1066–1071.
[49] A. Balamurugan, G. Sockalingum, J. Michel, J. Fauré, V. Banchet, L. Wortham, S. Bouthors, D. Laurent-Maquin, G. Balossier, Mater. Lett. 60 (2006) 3752–3757.
[50] L. Ji, W. Qiao, K. Huang, Y. Zhang, H. Wu, S. Miao, H. Liu, Y. Dong, A. Zhu, D. Qiu, Mater. Sci. Eng. C 75 (2017) 590–595.
[51] A.M. Putz, M.V. Putz, Int. J. Mol. Sci. 13 (2012) 15925–15941.
[52] J. Serra, P. González, S. Liste, C. Serra, S. Chiussi, B. León, M. Pérez-Amor, H. O. Ylänen, M. Hupa, J. Non-Cryst. Solids 332 (2003) 20–27.
[53] H. Aguiar, J. Serra, P. Gonzalez, B. Leon, J. Non-Cryst. Solids 355 (2009) 475–480.
[54] S. Martínez, F. Acción, F. Puertas, Mater. Constr. 42 (1992) 25–36.
[55] F. Rubio, J. Rubio, J.L. Oteo, Spectrosc. Lett. 31 (1998) 199–219.
[56] A. Tilocca, A.N. Cormack, N.H. de Leeuw, Chem. Mater. 19 (2007) 95–103.
[57] A. Tilocca, A.N. Cormack, J. Phys. Chem. B 111 (2007) 14256–14264.
[58] J.H. Lopes, E.M.B. Fonseca, I.O. Mazali, A. Magalhaes, R. Landers, C.A. Bertran, Mater. Sci. Eng. C Mater. Biol. Appl. 72 (2017) 86–97.
[59] E.M.J. Verbruggen, J.P. Rila, T.P. Traas, C.J.A.M. Posthuma-Doodeman, R. Posthumus, International and National Environmental Quality Standards for Substances in the Netherlands, National Institute for Public Health and the Environment, Netherlands, 2005.